Rapid Identification of Efficient Photocatalysts by Visualizing the Spatial Distribution of Photoinduced Charge Carriers

Tengfei Jiang, Jingying Wei, Jianyang Li, Huaiguo Xue, Jingqi Tian, Romain Gautier

Rapid identification of efficient photocatalysts by visualizing the spatial distribution of photoinduced charge carriers

Tengfei Jiang,[a] Jingying Wei,[a] Jianyang Li,[a] Huaiguo Xue,[a] Jingqi Tian,*[a] and Romain Gautier*[b]

[a] School of Chemistry and Chemical Engineering, Yangzhou University, 180 Siwangting Road, Yangzhou 225002, People's Republic of China, E-mail: jiangtengfei@yzu.edu.cn (T. Jiang); tianjq@yzu.edu.cn (J. Tian).

[b] Centre National de la Recherche Scientifique CNRS-IMN, 2 rue de la Houssinière, 44300, Nantes, France, E-mail: romain.gautier@cnrs-imn.fr (R. Gautier).

KEYWORDS: Identification of photocatalysts; Descriptor; Photoinduced charge carriers; Heterojunction photocatalysts; H_2 evolution.

ABSTRACT. The design of high-performance photocatalysts is of great importance for solar energy conversion. However, the rapid identification of efficient photocatalysts is challenging because of the complex dynamics of photoinduced charge carriers. Herein, we develop an experimental descriptor, the average fluorescence intensity (AFI), to rapidly identify the high-performance photocatalysts based on the fluorescence microscopic visualization of charge dynamics. As a proof-of-concept, $CuFeO_2$/ZIF-67 heterojunction was used to visualize the spatial distribution of photoinduced charges with identified diffusion length. Furthermore, a linear relationship was obtained between photocatalytic activities and the AFI, indicating an improved charge separation efficiency in the heterojunction responsible for an enhanced photocatalytic activity. This work provides a fundamental understanding of the dynamics of photoinduced charge carriers and offers a promising descriptor for the future design of efficient photocatalysts.

INTRODUCTION

The conversion of solar energy into chemical energy or high value-added chemicals by photocatalysis is an effective approach to utilize a clean energy while avoiding energy waste and environmental issues.[1] Unfortunately, most of the photocatalysts suffer from critical charge recombination, which severely restricts their large-scale applications.[2,3] Accordingly, developing an efficient strategy for catalyst design to overcome the charge separation bottleneck has a great value in both fundamental and applied research.[4] In this context, the heterojunction engineering has emerged as a promising strategy owing to the optimal charge separation by the built-in electric field between two semiconductors and the enlarged specific surface area.[5,6] Thus, the in depth understanding of the complex dynamic behavior of photogenerated charge could provide guidance for the identification of high-performance photocatalysts.[7,8,9] Therefore, it is necessary to deeply explore the dynamics of charge carriers, and establish an experimental descriptor between activity and charge behaviors to quickly identify high-performance catalysts.

Fluorescence microscopy visualization is a fast imaging method, which facilitates the exploration of charge carriers by using suitable probe molecules. Compared with conventional spectroscopy and electrochemical methods,[10,11] fluorescence microscopy visualization has advantages on studying spatial distribution and dynamics parameters of photoinduced charge carriers. Among the photocatalysts, the 2D heterojunctions have several fascinating merits including short carrier transfer distance from the bulk to the surface and reduced internal recombination of photoinduced charge carriers.[12,13,14] For these reasons, the 2D heterojunction is an interesting model to study charge dynamics. Recent efforts towards the 2D heterojunction lead to the discovery of numerous photocatalysts.[15,16] Among them, delafossite $CuFeO_2$ and Co-based ZIF-67 material show a great potential.[17,18,19].

In this article, we directly visualize the spatial distribution of photoinduced charge carriers in $CuFeO_2$/ZIF-67 heterojunction by fluorescence microscopy with two different fluorescent probe molecules. The designed 0D on 2D $CuFeO_2$/ZIF-67 heterojunction has distinct morphologies providing an easy to observe model for visualization. We found that the interfacial built-in electric field could operate the photoinduced holes and electrons distributed on different sites of $CuFeO_2$/ZIF-67 heterojunction, which improves the charge separation efficiency. Furthermore, we developed an experimental descriptor, the average fluorescence intensity (AFI), to rapidly identify high-performance photocatalysts based on charge dynamics. A linear relationship between the photocatalytic activities and the AFI demonstrates that the heterojunction improves charge separation efficiency, thus enhancing photocatalytic activity. As a proof of concept, the photocatalytic selective oxidation of benzyl alcohol (BA) to benzaldehyde (BAD) as well as photocatalytic hydrogen evolution reaction were selected to evaluate the activity of $CuFeO_2$/ZIF-67 heterojunction. Thus, we demonstrated that the photocatalyst with the optimal performance (quantum efficiency of 81.26% and 4.78% for BA conversion and H_2 evolution, respectively) was rapidly identified using the AFI descriptor.

RESULTS AND DISCUSSION

Our previous work showed that 2D $CuFeO_2$ nanosheets with a thickness of 40 nm could be prepared successfully, providing an appropriate template for the construction of heterojunctions.[20] Thus, in this work, 2D $CuFeO_2$/ZIF-67 heterojunctions with distinct morphological structure could be designed for visualizing the spatial distribution of photoinduced charge carriers. The detailed preparation of $CuFeO_2$ nanosheet are described in SI.

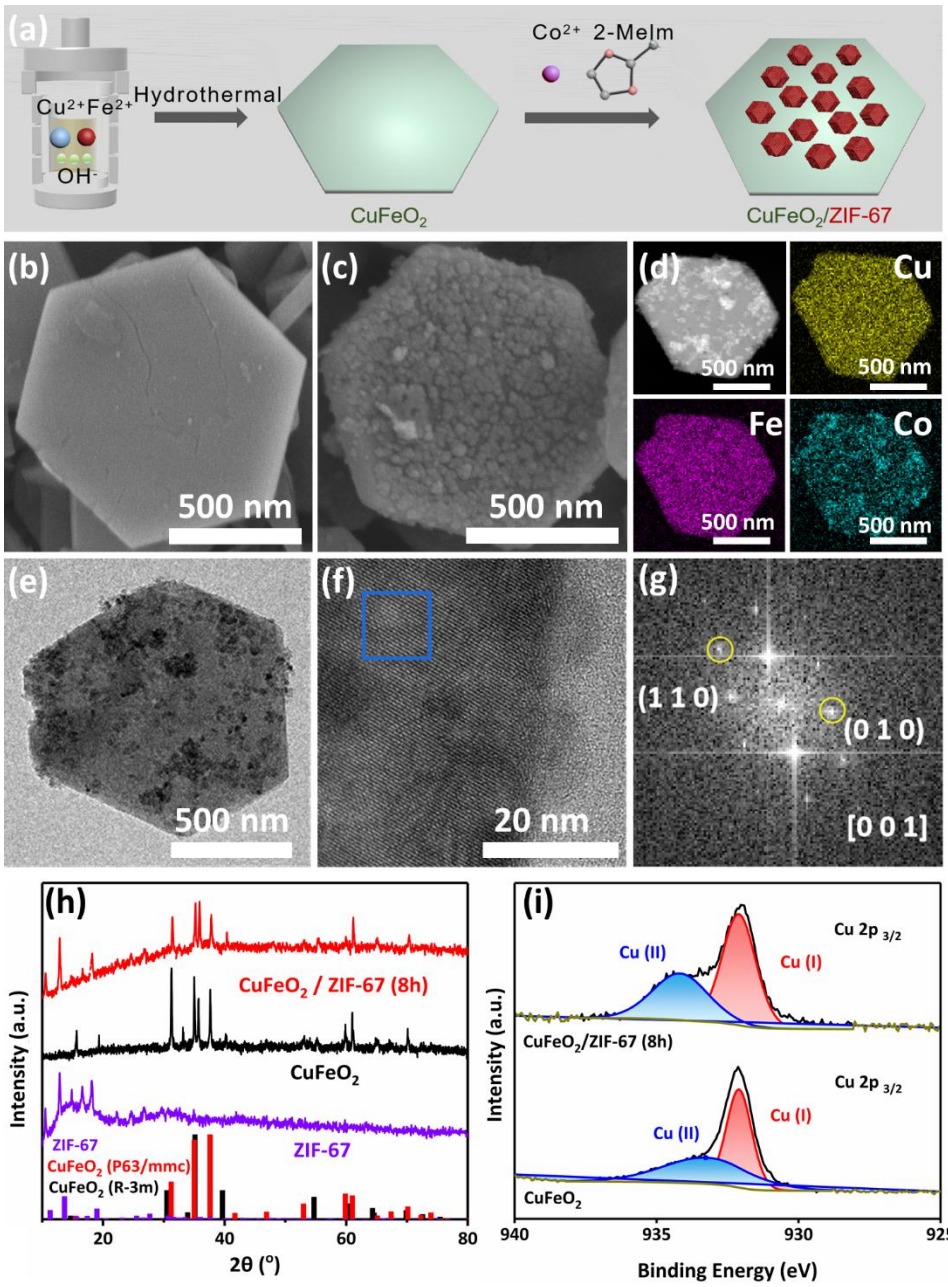

Figure 1. Synthesis route for $CuFeO_2$/ZIF-67 heterojunction (a); SEM of $CuFeO_2$ and $CuFeO_2$/ZIF-67 heterojunction (b, c); EDS mapping of $CuFeO_2$/ZIF-67 (8h) heterojunction (d); TEM (e), HRTEM (f), and FFT (g) images of $CuFeO_2$/ZIF-67 heterojunction; XRD patterns of $CuFeO_2$, ZIF-67, and $CuFeO_2$/ZIF-67 (8h) heterojunction (h); Cu 2p XPS spectra in pure $CuFeO_2$ and $CuFeO_2$/ZIF-67 (8h) heterojunction (i).

The synthesis route is schemed in Figure 1a. SEM images (Figure 1b, c, Figure S1) show that ZIF-67 nanoparticles are grown on the $CuFeO_2$ surface, and with the increase of reaction time from 4 to 8 hours, ZIF-67 nanoparticles with a mean particle size of ca. 50 nm are gradually covered on the surface of $CuFeO_2$ nanosheets. The as prepared $CuFeO_2$/ZIF-67 heterojunction remain of hexagon nanosheet morphology with a diameter of 400 nm and a thickness of 40 nm. Scanning TEM coupled with EDS elemental mapping (Figure 1d) show elemental Cu and Fe are uniformly distributed on the surface of the hexagonal substrate, while the distribution of Co element is more dispersed in small islands structure. Such observationproves the successful synthesis of $CuFeO_2$/ZIF-67 heterojunction. The specific surface area of $CuFeO_2$, ZIF-67, and $CuFeO_2$/ZIF-67 heterojunction are shown in Table S1. The TEM image reveals the hexagon nanosheet decorated with 30 nm size particles =on the surface (Figure 1e). The FFT patterns from the selected area in HRTEM image (Figure 1f) are indexed to the $CuFeO_2$ [001] zone axis (Figure 1g). The XRD diffraction peaks match perfectly with $CuFeO_2$ (JCPDS No. 75-2146, 79-1546) and ZIF-67 (CCDC No. GITTOT) without any impurities (Figure 1h). The XPS spectra (Figure S2) demonstrate the existence of Cu, Fe, Co, C, N, and O in $CuFeO_2$/ZIF-67 and Cu, Fe, C, and O in $CuFeO_2$. From the Cu 2p XPS spectra (Figure 1i), two contributions at 934.1 and 932.2 eV were attributed to Cu^{II} and Cu^{I}, respectively. After construction of the heterojunction, the peak area ratio of $Cu^{I}/(Cu^{I} + Cu^{II})$ increases from 50% to 60%, which indicates the electron transfer from ZIF-67 to $CuFeO_2$ resulting in the increase of Cu^{I}.

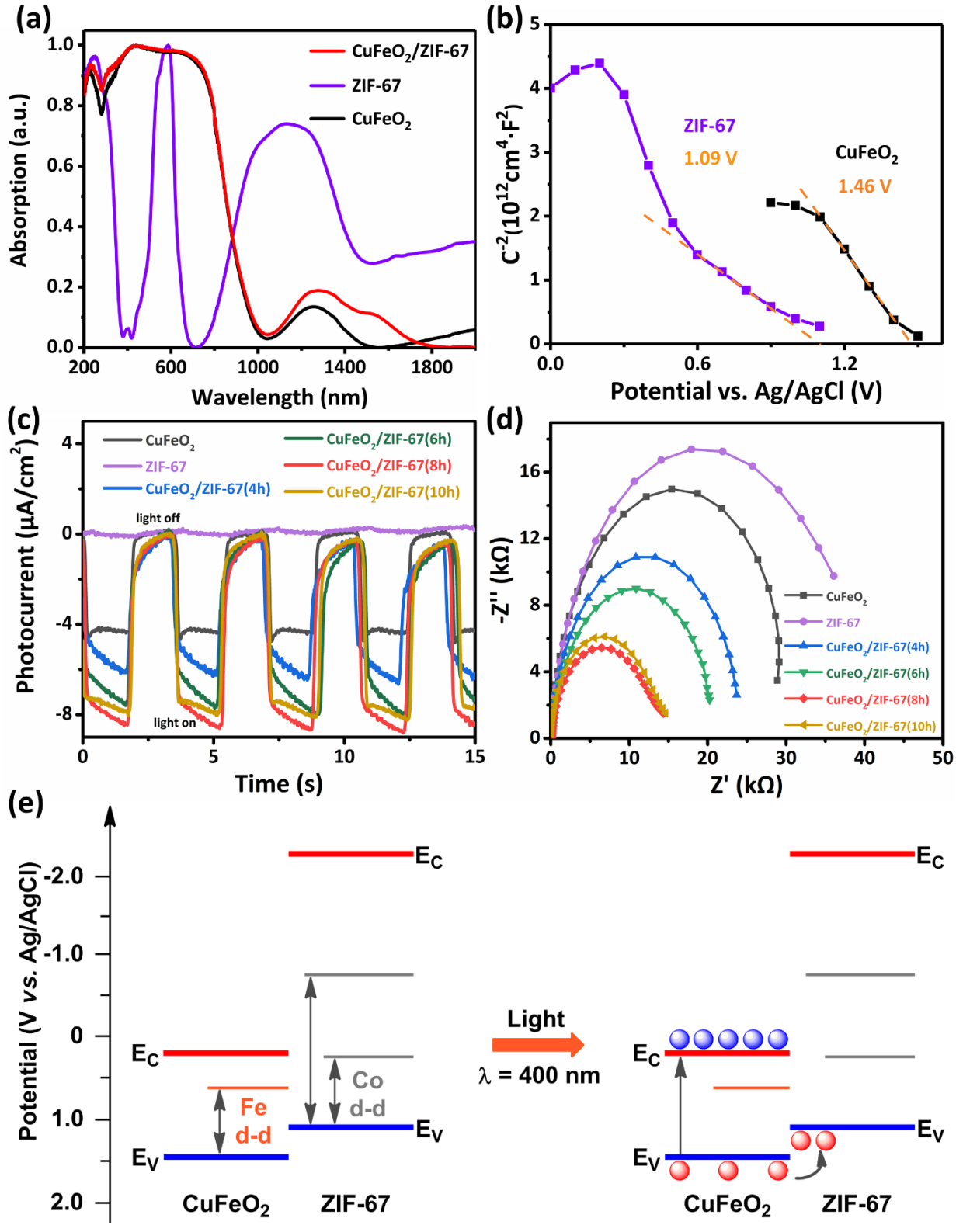
(a)
Absorption (a.u.)
Wavelength (nm)
CuFeO2/ZIF-67
ZIF-67
CuFeO2
(b)
C-2(1012cm4·F2)
Potential vs. Ag/AgCl (V)
ZIF-67
1.09 V
CuFeO2
1.46 V
(c)
Photocurrent (μA/cm2)
Time (s)
CuFeO2
ZIF-67
CuFeO2/ZIF-67(4h)
CuFeO2/ZIF-67(6h)
CuFeO2/ZIF-67(8h)
CuFeO2/ZIF-67(10h)
light off
light on
(d)
-Z'' (kΩ)
Z' (kΩ)
CuFeO2
ZIF-67
CuFeO2/ZIF-67(4h)
CuFeO2/ZIF-67(6h)
CuFeO2/ZIF-67(8h)
CuFeO2/ZIF-67(10h)
(e)
Potential (V vs. Ag/AgCl)
EC
EV
Fe d-d
Co d-d
CuFeO2
ZIF-67
Light
λ = 400 nm

Figure 2. The UV-vis-NIR absorption spectra of $CuFeO_2$, ZIF-67, and $CuFeO_2$/ZIF-67 heterojunction (8 h) (a); Mott-Schottky plots of $CuFeO_2$ and ZIF-67 in 0.5 M Na_2SO_4 (b); Chopped I-t curves (c) and electrochemical impedance spectra (d) of ZIF-67, $CuFeO_2$ and $CuFeO_2$/ZIF-67 heterojunction at -0.5 V vs. Ag/AgCl performed in 0.5 M Na_2SO_4 electrolyte; the schematic representation of energy band diagram with the calculated band gap and charge transfer process (e).

The optical UV-vis-NIR absorption spectra from 200 to 2000 nm are shown in Figure 2a. The $CuFeO_2$ sample presents two obvious absorption bands, including one in the UV-vis region (<1000 nm) and one in near IR region (1050-1500 nm), which are assigned to intrinsic band to band transition from Cu 3d and O 2p to Cu/Fe 3d orbitals, and d-d transitions at Fe^{III} site.[18,21] The Fe-O interatomic distances are comparable in $CuFeO_2$ (2.0559 Å, COD ID: 1533117) and in Fe_2O_3 (1.9443/2.1136 Å, COD ID: 2101167). The ZIF-67 sample exhibits three absorption regions: UV (<380 nm), visible (420-720 nm), and near IR (720-1400 nm), which are attributed to the LMCT transition, the higher-lying [$^4A_2(F) \rightarrow {}^4T_1(P)$] and lower-lying [$^4A_2(F) \rightarrow {}^4T_1(F)$] d-d ligand field transitions at Co^{II} site, respectively.[22] The absorption in visible region of green and yellow light makes the material of bluish violet color. Previous work reported that long-lived charge separation state occurs in ZIF-67 material after light irradiation, which is featured as semiconductor behavior strongly implying the potential application in photocatalysis.[22,23,24] The $CuFeO_2$/ZIF-67 heterojunction and $CuFeO_2$ have similar absorption features below 1000 nm, while the absorption intensity above 1000 nm is higher for $CuFeO_2$/ZIF-67 heterojunction due to the absorption of ZIF-67. The transformed Tauc plots give the energy level difference between the ground state and the excited state of $CuFeO_2$ and ZIF-67 as shown in Figure S3.

To obtain the valence band (VB) edges of $CuFeO_2$ and ZIF-67, Mott-Schottky plots were measured. Both plots show negative slops indicating p-type conductivity (Figure 2b). From the intercept of plots with X axis, the flatband potentials (regarded as the VB) can be measured at 1.46 and 1.09 V vs. Ag/AgCl for $CuFeO_2$ and ZIF-67, respectively. The photoelectrochemical characteristics of the $CuFeO_2$ and $CuFeO_2$/ZIF-67 heterojunction electrodes were analyzed as shown in Figure 2c. The $CuFeO_2$ and $CuFeO_2$/ZIF-67 heterojunction display an instant photocathodic response when the sample is illuminated. The $CuFeO_2$/ZIF-67 heterojunction shows higher photocurrent than $CuFeO_2$ electrode. In addition, the $CuFeO_2$/ZIF-67 (8h) heterojunction presents the highest photocurrent of -7.37 $\mu A/cm^2$, which demonstrates the presence of an enhanced charge separation in the heterojunction. The ZIF-67 exhibits no response, showing that a serious charge recombination exists in ZIF-67. The charge transfer behavior at the interface between photoelectrodes and electrolyte was investigated by electrochemical impedance spectroscopy (EIS) as shown in Figure 2d. For the photoelectrode prepared from the $CuFeO_2$/ZIF-67 heterojunction material, the $CuFeO_2$ particles are separated by ZIF-67, so the interfacial charge transfer within a single particle is included in the whole charge transfer channel of the photoelectrode. The interfacial charge transfer resistance within a single particle will affect the whole charge transfer resistance. So the EIS method can be used to analyze the interfacial charge transfer process in heterostructures. The $CuFeO_2$/ZIF-67 (8h) heterojunction shows a smaller semicircle diameter than other samples indicating a much lower charge-transfer resistance after heterojunction construction. Under the action of the interface electric field, the photogenerated electrons and holes are separated in different directions. This phenomenon inhibits recombination, improves the carrier life and enhances the photocatalytic efficiency. Additionally, the fluorescence spectra of $CuFeO_2$, ZIF-67, and $CuFeO_2$/ZIF-67

heterojunction were measured to illustrate the charge recombination process as shown in Figure S4. The $CuFeO_2$/ZIF-67 (8h) sample shows the weakest intensity among the different heterostructures indicating the enhanced charge separation efficiency benefited from the construction of heterojunction. Therefore, combined with the band gap from the Tauc plots (Figure S3), the conduction band (CB) is determined at 0.21 and -2.26 V vs. Ag/AgCl for $CuFeO_2$ and ZIF-67, respectively. $CuFeO_2$ has a lower CB and VB than ZIF-67. From these band gaps, a precise energy band diagram with the calculated band gap and charge transfer process can be proposed (Figure 2e). Under light (λ = 400 nm) irradiation, photoinduced holes transfer from the VB of $CuFeO_2$ to the VB of ZIF-67, which suppress the recombination of photoinduced charge.

To visualize the photoinduced charge transfer behavior, fluorescence microscopy was employed with amplex red and resazurin as probes of photoinduced holes and electrons, respectively.[25,26] The absorption and photoluminescence spectra of the probes and their fluorescence state are shown in Figure S5. The fluorescence microscopy images of different photocatalysts were measured via dispersing in amplex red or resazurin aqueous solution. Under the excitation wavelength of 400 nm, the nonfluorescent amplex red and resazurin molecules may capture, respectively, photoinduced holes and photoinduced electrons from pure $CuFeO_2$ nanosheet and convert to fluorescent resorufin (maximum emission wavelength of 610 nm). The monitor wavelength for the fluorescence images is from 559-689 nm. Although the fluorescence bands of resorufin and resazurin are overlapped partially (Figure S5), the fluorescence of resazurin is treated as the background and has been subtracted in the fluorescence images. The fluorescence intensity is proportional to the concentration of photoinduced charge carriers. Therefore, the probe molecule can detect the behaviour of photoinduced carriers at any site, and

allows to evaluate the photocatalytic activity of this site. With the help of probe molecules, we successfully visualize the distribution of photoinduced charge carriers in $CuFeO_2$ sample (fluorescence microscopy images with electrons and holes probe molecules shown in Figure 3). The transition processes of nonfluorescent and fluorescent states of the probe molecules are illustrated in Figure 3a.

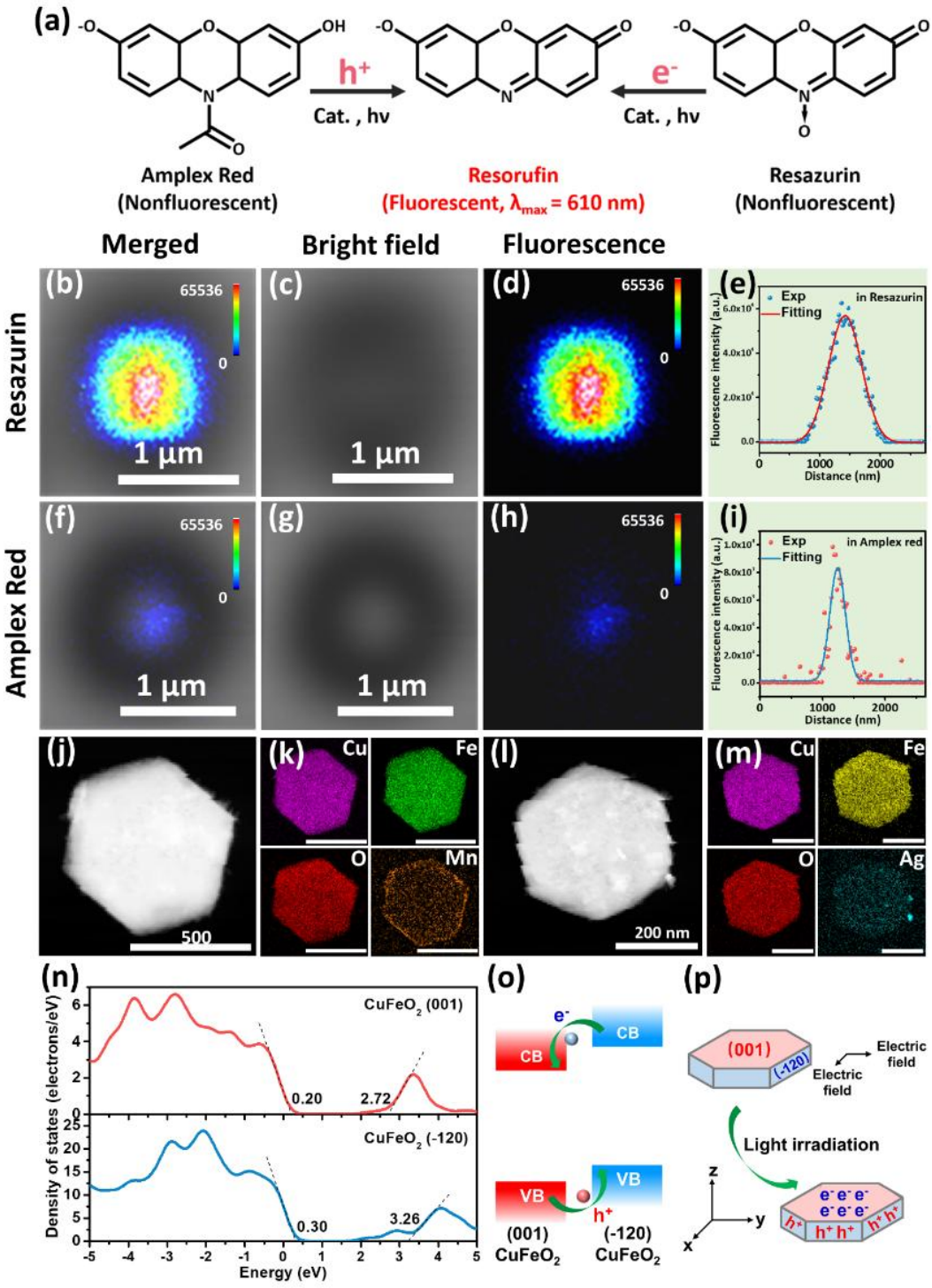

Figure 3. Transition processes of nonfluorescent and fluorescent states of probe molecules (a); fluorescence microscopy images of $CuFeO_2$ nanosheet in 50 nM resazurin (b-d); fluorescence intensity from line scanning of fluorescence microscopy images vs. the distance by using

resazurin (e); fluorescence microscopy images of $CuFeO_2$ nanosheet in 50 nM amplex red (f-h); fluorescence intensity from line scanning of fluorescence microscopy images vs. the distance by using amplex red (i); TEM (j) and element mapping images (k) of $CuFeO_2$ after photo-deposition experiment by using Mn^{2+}; TEM (l) and element mapping images (m) of $CuFeO_2$ after photo-deposition experiment by using Ag^{+}; calculated DOS of $CuFeO_2$ (001) and (-120) facets (n); schematic diagram of energy level (o) and photoinduced charge transfer process (p).

By using the electron probe molecule of resazurin, a strong fluorescence signal is observed for the $CuFeO_2$ nanosheet as shown in Figure 3b-d. The fluorescence intensity from line scanning of fluorescence microscopy images vs. the distance by using resazurin is shown in Figure 3e. When using the amplex red (probe of holes), a weak fluorescence signal is observed (Figure 3f-h) as few photoinduced holes are located at the surface. The fluorescence intensity from line scanning of fluorescence microscopy images vs. the distance by using amplex red is shown in Figure 3i. $CuFeO_2$ is a p-type semiconductor with a downward surface band bending. Accordingly, under the effect of the built-in electric field in the surface space charge region, the photoinduced electrons shift to the surface and the photoinduced holes move to the bulk. Furthermore, the fluorescence intensity at the center of $CuFeO_2$ particles is higher than that at the edge, and the uneven distribution of fluorescence intensity originates from the uneven charge concentration distribution at $CuFeO_2$ (001) facets. According to the theory of semiconductor physics, the behavior of excess carriers with time and in space in the presence of electric fields and density gradients are described by the Haynes-Shockley model[27]. In such conditions, the continuity equation is expressed as:

$$\frac{\partial \Delta n}{\partial t} = D\frac{\partial^2 \Delta n}{\partial x^2} - \mu\varepsilon\frac{\partial \Delta n}{\partial t} - \frac{\Delta n}{\tau} \quad (1)$$

Where Δn, D, μ, τ and ε corresponds to the carrier concentration, diffusion constant, mobility, lifetime, and the strength of internal electric field, respectively. In our model, a horizontal polarized electric field (HPEF), which originates from the difference of energy levels between $CuFeO_2$ (001) and (-120) facets, exists and drives the photoinduced charge carriers movements in x-y plane (Figure 3p). The HPEF is also confirmed by the heterogeneous distribution of the fluorescence intensity. In other words, if the HPEF is absent, the fluorescence intensity should be homogeneous as the particles are excited at any sites. The solution of equation (1) is:

$$\Delta n = \frac{N_n}{\sqrt{4\pi D t}} exp\left[-\frac{(x-\mu\varepsilon t)^2}{4Dt}\right] exp\left[-\frac{t}{\tau}\right] \quad (2)$$

Equation (2) could be simplified as:

$$\Delta n \propto e^{-\frac{(x-\mu\varepsilon\tau)^2}{4D\tau}} \quad (3)$$

It can be seen that the carrier concentration distribution satisfies the Gaussian function. In the line scanning of fluorescence microscopy images, the fluorescence intensity is proportional to carrier concentration, which also agrees with the Gaussian distribution:

$$\Delta n \propto I \propto \frac{A}{\sigma\sqrt{2\pi}} e^{\left(-\frac{(x-x_C)^2}{2\sigma^2}\right)} \quad (4)$$

Where A is a constant, x is the variable, x_c is the mean, and σ is the standard deviation. By comparing the equation (3) and (4), the following equation is obtained:

$$D\tau = \frac{\sigma^2}{2} \quad (5)$$

So the carrier diffusion length (L) is extracted from the standard deviation:

$$L = \sqrt{D\tau} = \frac{\sigma}{\sqrt{2}} \quad (6)$$

The L value of pure $CuFeO_2$ obtained from the Gaussian fitting shown in Figure 3e and 3i are 195.17 nm and 87.77 nm for photoinduced electrons and holes, respectively. Photo-deposition experiments were carried out to further confirm the dynamic behavior of photoinduced charge carriers in this model by using Mn^{2+} and Ag^{+} as hole and electron probe, respectively. The element mapping images show that MnO_x and Ag nanoparticles deposited preferentially to deposit on side facets and top facets, respectively (Figure 3j-m). This distribution indicates that (-120) and (001) facets are enriched in holes and electrons, respectively. Additional density functional theory (DFT) calculations were carried out to explain the charge dynamics. The calculated DOS confirms that the conduction band and valence band of $CuFeO_2$ (001) face is lower than the ones of the (-120) face (Figure 3n). Such phenomenon generates a facet junction between the two facets. The difference of energy levels between the two facets provides the driving force, which lead to the photoinduced electrons transfer from (-120) to (001) face, and the photoinduced holes transfer from (001) to (-120) face (Figure 3o, p).

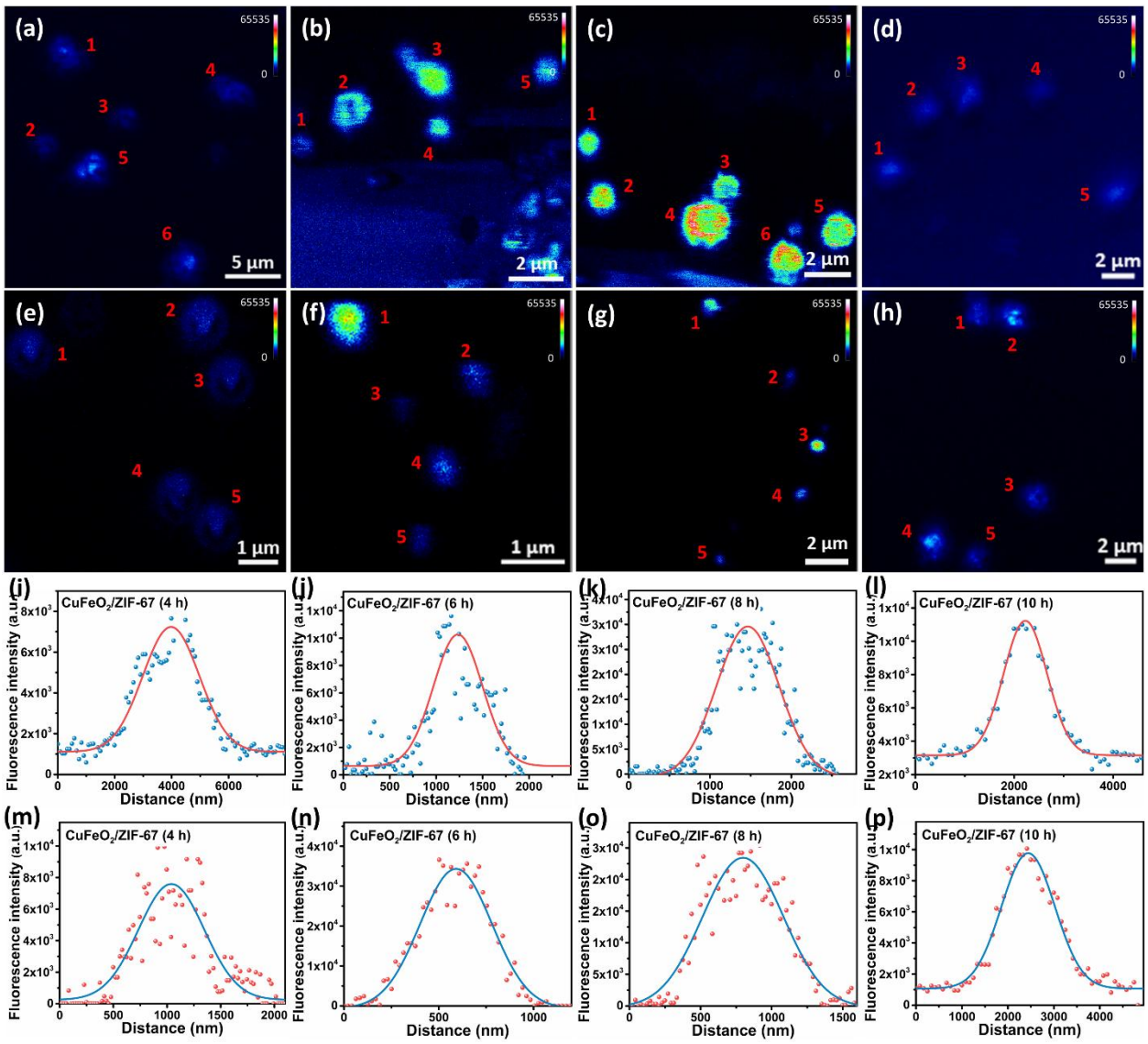

Figure 4. Fluorescence microscopy images of $CuFeO_2$/ZIF-67 (4, 6, 8, 10 h) heterojunction samples in 50 nM resazurin (a-d) and 50 nM amplex red (e-h) aqueous solution; the line scanning of fluorescence microscopy images of the particle 1 derived from (a)-(d) by using resazurin (i)-(l); the line scanning of fluorescence microscopy images of the particle 1 derived from (e)-(h) by using amplex red (m)-(p).

We further visualize the distribution of photoinduced charge carriers in different $CuFeO_2$/ZIF-67 heterojunctions, and carried out a statistical analysis from the fluorescence

microscopy images of at least three particles for each sample (Figure 4). In comparison to $CuFeO_2$, the fluorescence intensity distribution for $CuFeO_2$/ZIF-67 heterojunctions using electron probe molecule remains uneven with the central region exhibiting a higher intensity of the fluorescence (Figure 4a-d). Interestingly, when using holes probe molecules, an obvious fluorescence signal region located on the center of the heterojunction can be observed for all $CuFeO_2$/ZIF-67 samples (Figure 4e-h). This observation indicates that photoinduced holes populate the center of the catalyst under the action of the interface built-in electric field and the facet junction of $CuFeO_2$ simultaneously. ZIF-67 particles are located on the surface of $CuFeO_2$ nanosheet, which proves that the photoinduced holes are localized on the outer ZIF-67 particles. For $CuFeO_2$/ZIF-67 (10 h), the excess quantity of ZIF-67 hinders the absorption of light in the heterojunction region decreasing the charge concentration. Such phenomenon results in a weaker fluorescence signal in comparison to $CuFeO_2$/ZIF-67 (8 h). The line scanning of fluorescence microscopy images are shown in Figure 4i-p. The carrier diffusion length was obtained from the line scanning of fluorescence microscopy images as shown in Table S2, and the L value for $CuFeO_2$/ZIF-67 heterojunctions are longer than the L value of pure $CuFeO_2$. It should be noted that, the regions concentrated in electrons prefer to undergo catalysis reduction reaction, while the regions concentrated in holes are more inclined to catalysis oxidation reaction.[28,29] All these observations promise that such $CuFeO_2$/ZIF-67 heterojunctions are favorable catalysts toward photocatalytic reactions.

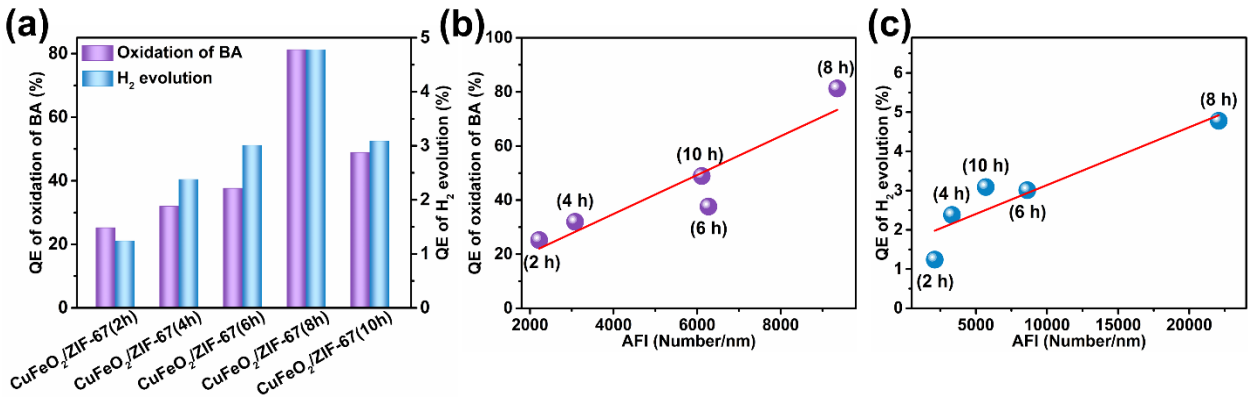

Figure 5. The quantum efficiencies (QE) of oxidation of BA and H_2 evolution of $CuFeO_2$/ZIF-67 heterojunctions (2, 4, 6, 8, 10 h) (a); the QE of BA conversion versus descriptor (AFI) (b); the QE of H_2 evolution versus descriptor (AFI) (c).

As a proof of concept, the performance of photocatalytic selective oxidation of BA and H_2 evolution performance of the different as prepared heterojunctions were analyzed. At the beginning of the reaction, reactant molecules are adsorbed on different catalyst surface sites. The DFT calculations indicate that the adsorption energies of BA/H_2O are comparable for $CuFeO_2$ and ZIF-67 surfaces (Figure S6). Therefore, one can conclude that the photocatalytic activity mainly depends on the efficiency of photoinduced charge separation. The photocatalytic quantum efficiencies of the selective oxidation of BA and H_2 evolution are gradually increased from $CuFeO_2$/ZIF-67 (4 h) heterojunction to $CuFeO_2$/ZIF-67 (8 h) heterojunction (Figure 5a). The $CuFeO_2$/ZIF-67 (8 h) heterojunction exhibits the highest quantum efficiency (QE) of 81.26% and 4.78% for the photocatalytic selective oxidation of BA and H_2 evolution, respectively. The quantum efficiency for $CuFeO_2$/ZIF-67 (10 h) decreases, which resulted from the excess of ZIF-67 particles accumulated on the $CuFeO_2$ surface as this excess hinders the light absorption of $CuFeO_2$, weakens the effect of the heterojunction region and thus reduces the charge separation efficiency. The photocatalytic selective oxidation of BA is the thermodynamically downhill

reaction, and the photocatalytic H_2 evolution is thermodynamically uphill reaction (regarded as photosynthesis). Although the two types of reactions are obviously different in thermodynamics, from the material point of view, the considerations of photocatalyst properties, such as light absorption, charge separation and charge transfer, are analogous.[30] The recombination process of photoinduced charge carriers is important for photocatalysis, which affects the lifetime and the average distance of excess minority carriers from the location where the charge carriers are generated to the location where they are utilized.[31]

To identify a descriptor for the $CuFeO_2$/ZIF-67 heterojunction photocatalysts, we examined the relationship between the catalytic activities and the photoinduced charge carrier behavior. As an important elementary step in photocatalytic reaction, charge separation is crucial for increasing the performance of photocatalyst. Thus, a descriptor is desirable to optimize the charge separation efficiency and photocatalytic performance. The carrier diffusion length determines whether electron/hole created deeper in the bulk material can reach the surface, and the carrier concentration dominates the quantity of the electron/hole participating in the photocatalytic reaction.[32,33] Therefore, a new experimental descriptor, the average fluorescence intensity (AFI), which quantifies the diffusion length and concentration of photoinduced charge carriers simultaneously, is proposed to rationalize the catalytic activity trends. The AFI is defined as the integral of line scanning curve divided by distance, which meets the above-mentioned requirements. The physical meaning of AFI is the number of photoinduced charge carriers per unit length distance on the surface (Number/nm). The statistical AFI values of different $CuFeO_2$/ZIF-67 heterojunction samples are shown in Table S3. An excellent linear relationship between BA conversion and the AFI, as well as between H_2 evolution and the AFI, can be observed (Figure 5b, 5c), suggesting that the AFI can serve as a descriptor for predicting

the photocatalytic performance of heterojunction photocatalysts. The $CuFeO_2$/ZIF-67 (8 h) exhibits the highest AFI and shows the highest catalytic activity. Other samples with the shorter or longer growth time of ZIF-67 display weaker AFI, because of a lack of ZIF-67 leading to an insufficient photoinduced charge carriers generation or an excess of ZIF-67 leading to an insufficient light transmission reducing the action range of the junction region. All these results successfully demonstrated that the AFI is a practical descriptor for rapidly identifying efficient photocatalysts in both thermodynamically uphill and downhill reactions.

CONCLUSIONS

In summary, we focused on visualizing the distribution of photoinduced charge carriers in $CuFeO_2$/ZIF-67 heterojunction by fluorescence microscope with probe molecules. The heterojunction enhanced the separation efficiency of photoinduced charge carriers under the effect of interfacial built-in electric field, which improved the carrier diffusion length and concentration. Furthermore, we reveal that AFI can be used as an experimental descriptor to rapidly identify the high-performance photocatalyst. Thus, heterojunction samples with different AFI are demonstrated to display photocatalytic performance following the trends of $CuFeO_2$/ZIF-67 (2 h) < $CuFeO_2$/ZIF-67 (4 h) < $CuFeO_2$/ZIF-67 (6 h) < $CuFeO_2$/ZIF-67 (10 h) < $CuFeO_2$/ZIF-67 (8 h). Thus, we believe that the AFI could be a promising descriptor for the future screening of potential photocatalysts.

EXPERIMENTAL

Preparation of $CuFeO_2$ nanosheet.

The $CuFeO_2$ nanosheet was prepared by hydrothermal method based on our previous work.[20] More details are shown in Supporting Information (SI).

Preparation of $CuFeO_2$/ZIF-67 heterojunction.

First, 0.65 mmol $CuFeO_2$, 0.1 mmol $Co(NO_3)_2 \cdot 6H_2O$ and 2 mmol 2-methylimidazole were dispersed in 10 mL of DI water under stirring. Next, the mixture was transferred into a Teflon-lined stainless autoclave heating at 120 ^oC for 4, 6, 8 h to synthetize the heterojunction samples, which were named as $CuFeO_2$/ZIF-67 (4/6/8 h). Finally, the products were washed three times with water and ethanol, respectively and dried at 80 ^oC for 12 h. ZIF-67 was also prepared in the absence of $CuFeO_2$ under the same condition.

Characterization.

Scanning electron microscopy (SEM) images were obtained using a Zeiss Supra 55 electron microscope. High resolution transmission electron microscopy (HRTEM) characterizations were performed using a Tecnai G2 F30 S-TWIN transmission electron microscope operated at 200 kV. X-ray diffraction (XRD) patterns of the products were recorded using a Bruker D8 Focus diffractometer by using Cu Kα radiation (λ□= 1.54178 Å). X-ray photoelectron spectroscopy (XPS) spectra were obtained using an ESCALAB 250Xi Thermo Scientific X-ray photoelectron spectrometer. The $CuFeO_2$/ZIF-67 based work electrodes were fabricated using a dip-coating method. Typically, 0.008 g of the $CuFeO_2$ material was added in 5 mL of ethylene glycol monomethylether solution under ultrasound. Then, the sample suspension was dropped onto the FTO substrate and dried at 90 ^oC following a heating at 200 ^oC in a tube furnace for 30 min under N_2 atmosphere. Photoelectrochemical measurements were performed in a three-electrode system using an electrochemical workstation (Autolab).

Fluorescence microscopy imaging.

The catalysts powder (10 mg) was dispersed in 1 mL of ethanol and was sonicated for 1 minute. A portion (10 μL) of the above colloidal suspension was then dipped onto a cleaned glass slide heat at 90 ^{o}C to remove the ethanol getting a well dispersed catalysts particles layer. A portion (10 μL) of 50 nM resazurin/amplex red aqueous solution was then dipped onto the above prepared catalysts layer, and the liquid drop was carefully covered with a glass coverslip avoiding any gas bubbles. Then the catalysts on glass slide were used to perform the fluorescence microscopy imaging. A Zeiss LSM 880 NLO two-photon laser confocal microscopy system was used consisting of a Zeiss Axio Imager 2 optical microscope with oil-immersion objective lens (×100). The resolution limit of the fluorescence microscopy (ZEISS LSM 880 NLO, with the commercial ZEISS Airyscan detrctor) is of 130 nm in x, y and 350 nm in z. (https://www.zeiss.com) The operating software has the function of image magnification by adjusting the zoom settings, which could increase the magnification to see more details without objective change. To conclude, based on the above information, it is possible to identify the charge separation in a micro-sized particle. The well-isolated, non-aggregated catalyst particles visualized by bright field microscopy imaging were selected as regions of interest. Two photon laser line was typically used while recording the fluorescence images. Fluorescence images were analysed by ZEN software, and the line scanning of fluorescence microscopy images were obtained.

Photocatalytic reaction.

The photocatalytic reaction was carried out in a 30 mL quartz test bottle with a diameter of 26 mm and the light source is a 450 nm LED with light intensity of 17.93 W/m^2. The photocatalytic

selective oxidation of BA was carried out under air atmosphere by dispersing 30 mg catalyst in 5 mL of DMF with 1 mmol BA and 1.5 mg KOH, and the reaction time is 4 h. The BAD yields were determined by gas chromatography-mass spectrometry (Agilent 7890B). The photocatalytic hydrogen evolution reaction was carried out by dispersing 30 mg catalyst in 60 mL of 10% triethanolamine aqueous solution and the reaction time is 1.5 h. The H_2 evolution rate was determined by gas chromatography (GC-2014C). The quantium efficiency is calculated by the following equation[34],[35]:

$$\mathrm{QE} = 2 \times \frac{N(Product)}{N(Photons)}$$

where N(Product) and N(Photons) denote the number of product molecules (BAD or H_2) and the number of photons reaching the surface of the reaction solution, respectively.

DFT calculation.

The electronic structure of the system was investigated based on the DFT approach with the CASTEP program. Both structures were optimized at the generalized gradient approximation (GGA) level with Perdew–Burke–Ernzerhof (PBE) exchange–correlation functional and the ultra-soft pseudopotentials. To obtain the density of states (DOS) of $CuFeO_2$, we performed the PBE + U calculations with a value of U = 4.1 eV for the Fe 3d states, which is in agreement with previous reports for Fe atoms.[36] For geometry optimization, ultra-soft pseudopotentials with a kinetic energy cut-off of 351 eV and a G-centered 2×2×1 k-point mesh for sampling the Brillouin zone. During the optimization, the lattice parameters were fixed and only the atoms were allowed to relax. The vacuum layer of the models is set to be 15 Å to minimize the interaction between the periodic images.

ASSOCIATED CONTENT

Supporting Information. This material is available free of charge via the Internet at http://pubs.acs.org. Experimental details, SEM, XPS spectra, Tauc plots, fluorescence spectra, UV-vis-NIR absorption spectra, fluorescence microscopy images, DFT results and gas chromatograms data.

AUTHOR INFORMATION

Corresponding Authors

Tengfei Jiang - School of Chemistry and Chemical Engineering, Yangzhou University, 180 Siwangting Road, Yangzhou 225002, People's Republic of China, E-mail: jiangtengfei@yzu.edu.cn (T. Jiang);

Jingqi Tian - School of Chemistry and Chemical Engineering, Yangzhou University, 180 Siwangting Road, Yangzhou 225002, People's Republic of China, E-mail: tianjq@yzu.edu.cn (J. Tian);

Romain Gautier - Centre National de la Recherche Scientifique CNRS-IMN, 2 rue de la Houssinière, 44300, Nantes, France, E-mail: romain.gautier@cnrs-imn.fr (R. Gautier).

Author Contributions

Tengfei Jiang conceived and designed the experiments, analysed the data, and wrote the paper. Jingying Wei performed the experiments and revised the manuscript. Jianyang Li performed the experiments and collected the data. Huaiguo Xue designed the project and revised the manuscript. Jingqi Tian conceived and designed the experiments, and revised the manuscript. Romain Gautier conceived and designed the experiments, and revised the manuscript.

Notes

The authors declare no competing financial interest.

SUPPORTING INFORMATION

Experimental

Preparation of $CuFeO_2$ nanosheet.

A mixture of 1 mmol $CuSO_4 \cdot 5H_2O$, 1 mmol $FeSO_4 \cdot 7H_2O$, and 10 mL sodium alginate of 5 g/L were dissolved into 10 mL of deionized water by ultrasonic stirring for 10 min. The mixture was added in a Teflon-lined autoclave (50 mL), and then adding 10 mL 10 M NaOH into the autoclave and ultrasonic stirring for 5 min and putting the autoclave into drying oven at 160 ^oC for 6 h. Finally, the synthesized nanoflakes were washed three times with water and ethanol and dried at 80 ^oC for 12 h.[20]

RESULTS AND DISCUSSION

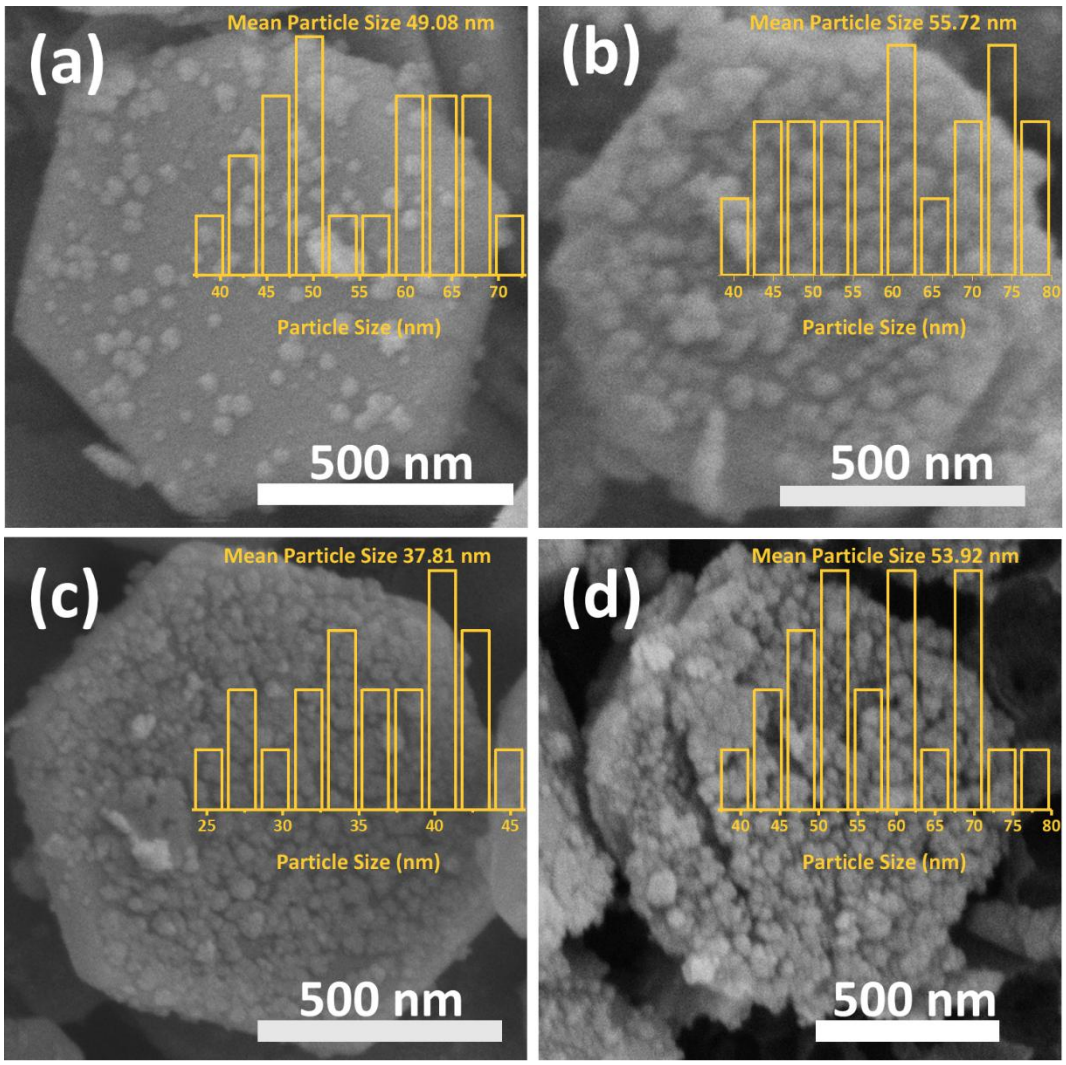

Fig. S1. SEM images of $CuFeO_2$/ZIF-67 (4h) (a), $CuFeO_2$/ZIF-67 (6h) (b), $CuFeO_2$/ZIF-67 (8h) (c), and $CuFeO_2$/ZIF-67 (10h) (d).

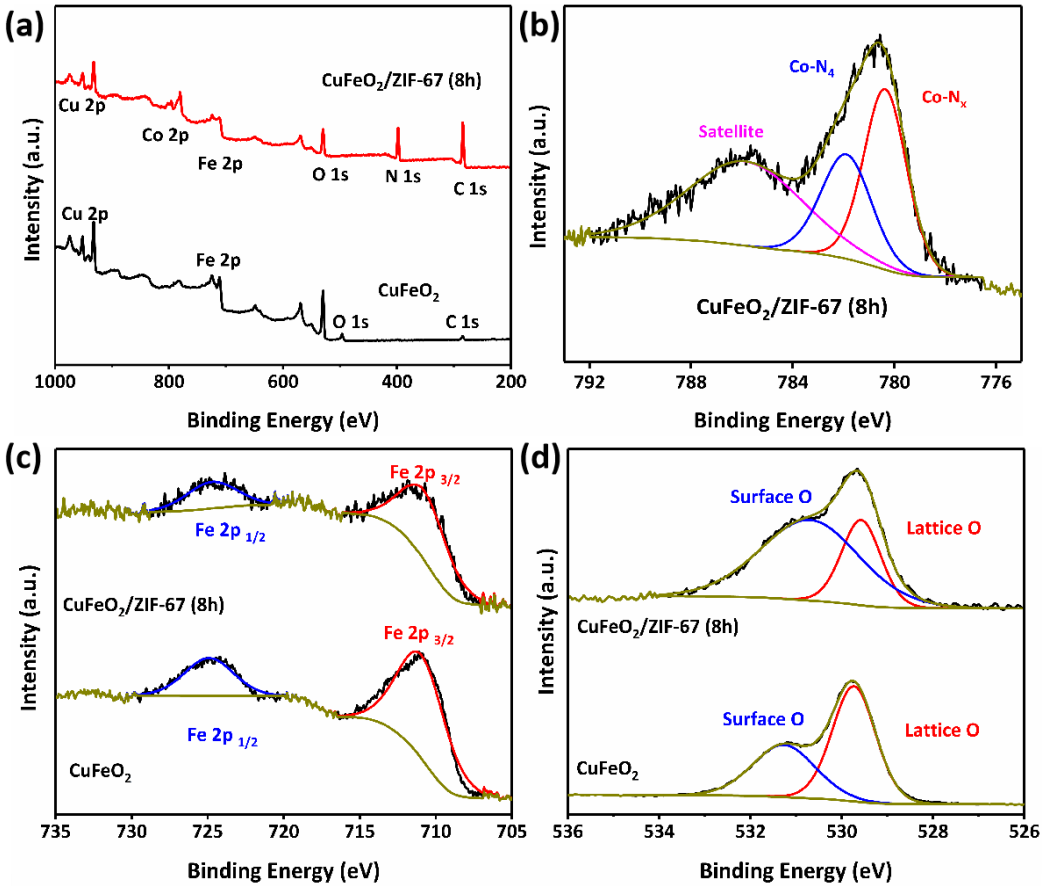

Fig. S2. XPS survey spectrum of $CuFeO_2$/ZIF-67 and pure $CuFeO_2$ (a); Co 2p spectrum in $CuFeO_2$/ZIF-67 (b); Fe 2p spectra in pure $CuFeO_2$ and $CuFeO_2$/ZIF-67 (c); O 1s spectra in pure $CuFeO_2$ and $CuFeO_2$/ZIF-67 (d).

The XPS survey spectra (Fig. S2a) demonstrate the existence of Cu, Fe, Co, C, N, and O in $CuFeO_2$/ZIF-67 and Cu, Fe, C, and O in $CuFeO_2$. From the Co 2p XPS (Fig. S2b), the contribution at 781.1 eV was attributed to fully coordinated cobalt within the Co-N_4 environment.[37],[38]. The observable satellite features at 786 eV suggest the valence state of cobalt is Co^{II}. The Fe 2p XPS peak at 710.8 eV (Fig. S2c) are contributed to Fe^{III}. From the O 1s XPS (Fig. S2d), two contributions at 531.8 and 529.5 eV were attributed to the surface hydroxyl and lattice oxygen, respectively. Thus, the increased surface hydroxyl in $CuFeO_2$/ZIF-67 is mainly attributed to the adsorbed O-species.

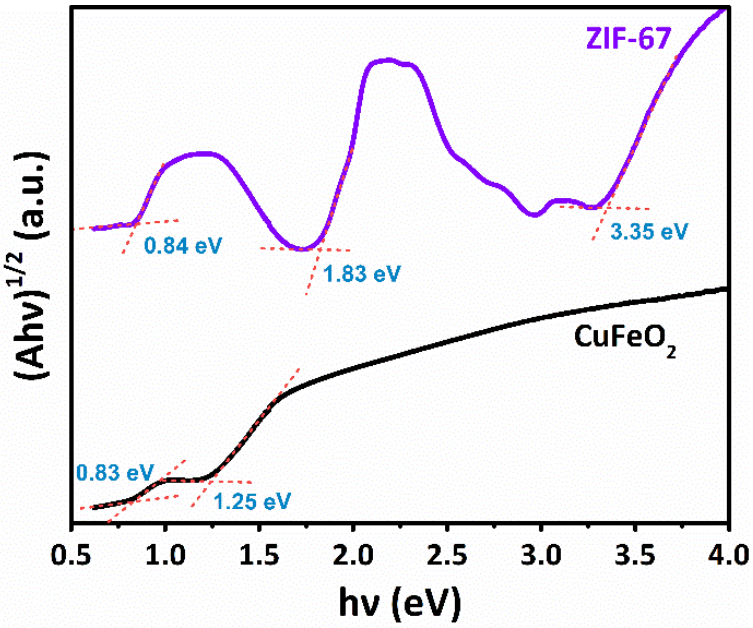

Fig. S3. Tauc plots of $CuFeO_2$ and ZIF-67 from UV-vis-NIR spectra and the intercept between absorption band edge and baseline.

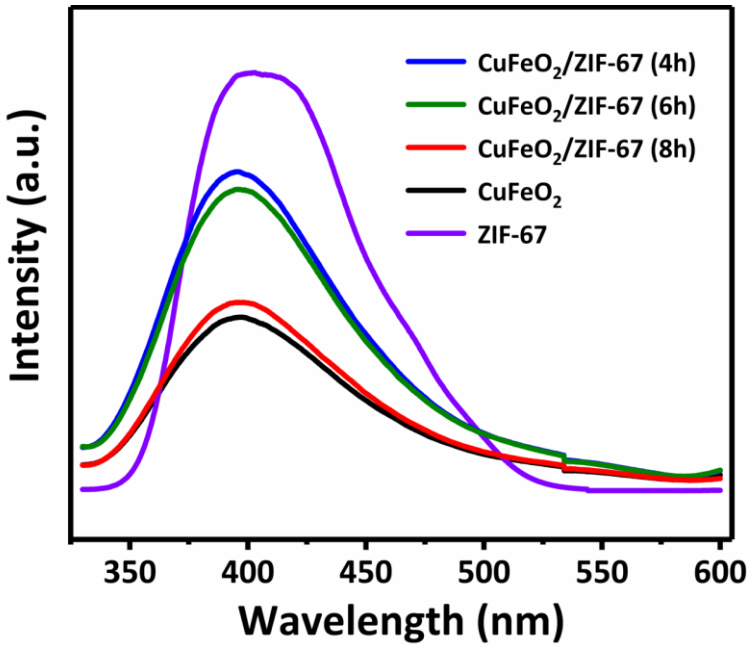

Fig. S4. Fluorescence spectra of ZIF-67, $CuFeO_2$ and $CuFeO_2$/ZIF-67 heterostructure dispersed in DMF at the excitation wavelength of 330 nm.

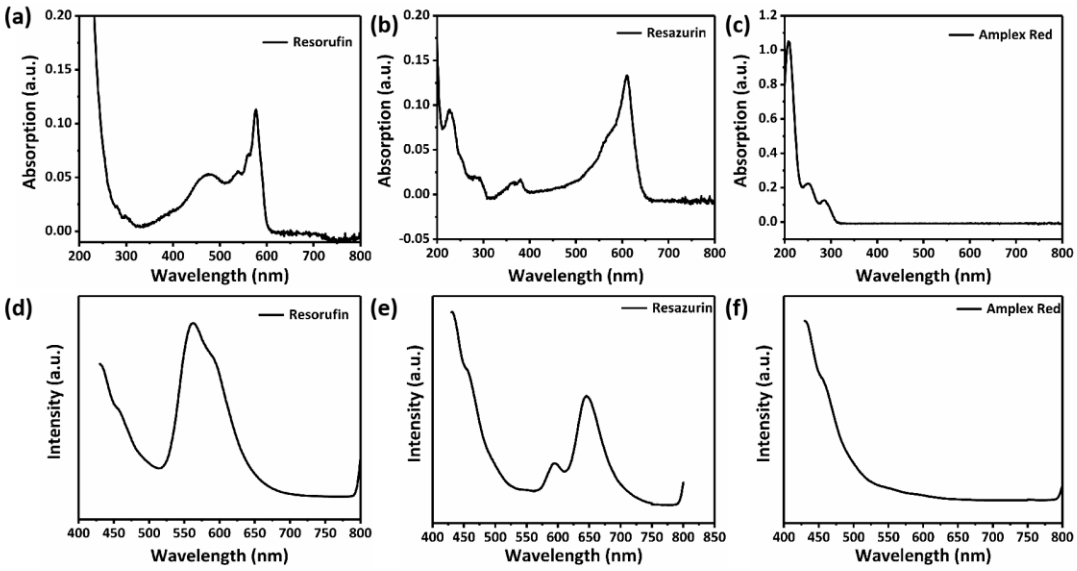

Fig. S5. The UV-vis-NIR spectra (a-c) and PL spectra with λ_{EX}=400 nm (d-f) of 25 nM Resorufin, Resazurin and Amplex Red ethanol solution.

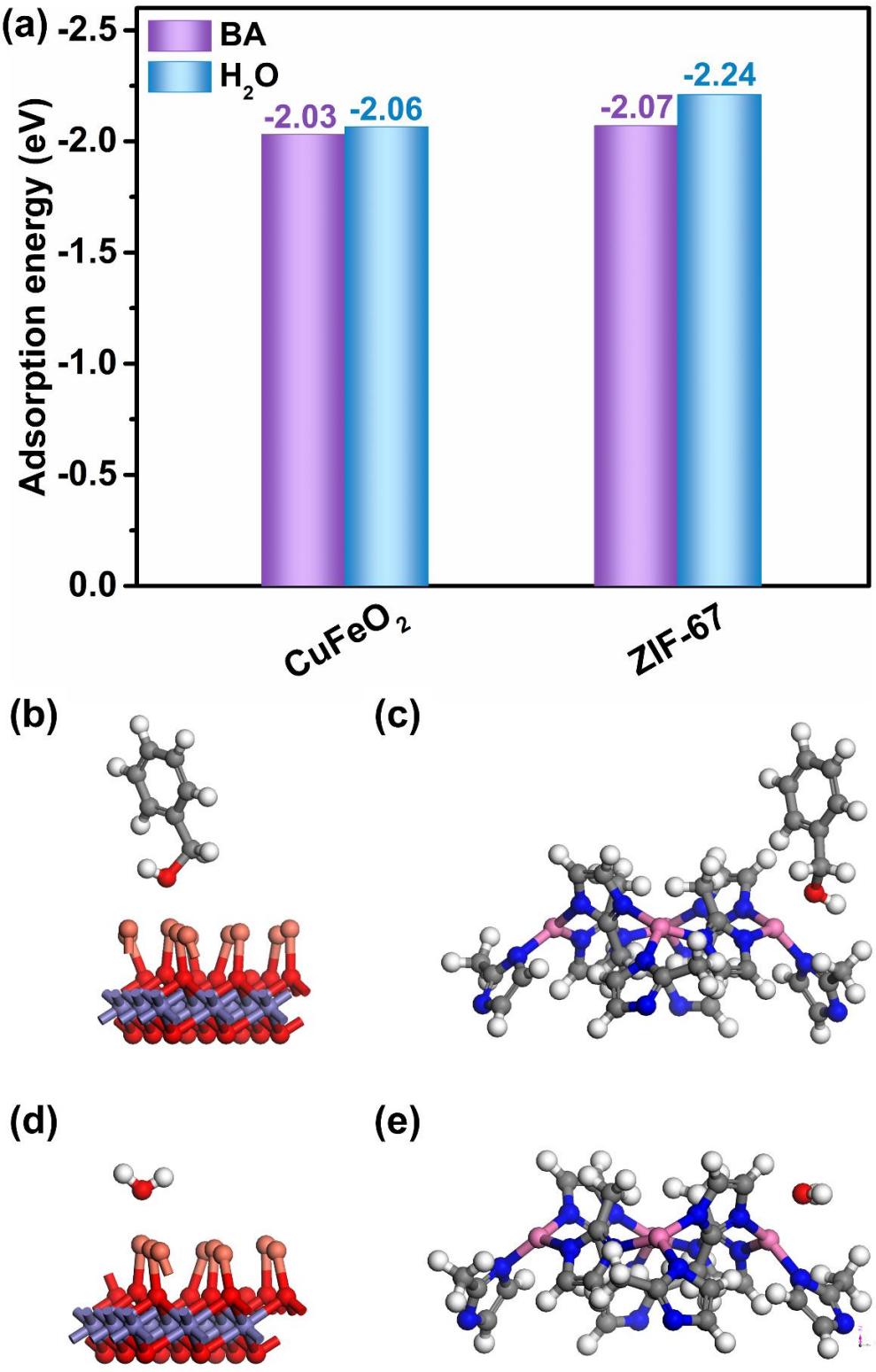

Fig. S6. DFT calculated adsorption energy of BA and H_2O on catalyst surfaces (a); the calculated adsorption configurations of BA and H_2O on catalyst surfaces (b-e).

Table S1. Specific surface area, pore volume, and average pore size of $CuFeO_2$, ZIF-67, and $CuFeO_2$/ZIF-67 heterojunction samples.

Samples	Specific surface area (m^2/g)	Pore volume (cm^3/g)	Pore size (nm)
$CuFeO_2$	18.411	0.081	3.934
ZIF-67	1122.223	0.603	2.486
$CuFeO_2$/ZIF-67 (4h)	25.730	0.111	3.133
$CuFeO_2$/ZIF-67 (6h)	49.040	0.165	3.317
$CuFeO_2$/ZIF-67 (8h)	64.382	0.285	3.499
$CuFeO_2$/ZIF-67 (10h)	73.249	0.265	3.133

Table S2. The carrier diffusion length of different $CuFeO_2$/ZIF-67 heterojunction samples.

Sample	Carrier diffusion length (L, nm)	
	in Resazurin	in Amplex red
$CuFeO_2$	195.17	87.77
$CuFeO_2$/ZIF-67 (4 h)	659.31	192.33
$CuFeO_2$/ZIF-67 (6 h)	299.46	100.08
$CuFeO_2$/ZIF-67 (8 h)	464.68	160.99
$CuFeO_2$/ZIF-67 (10 h)	344.21	378.71

Table S3. The statistical AFI values of different $CuFeO_2$/ZIF-67 heterojunction samples.

Sample	Statistical AFI (Number/nm)	
	in Resazurin	in Amplex red
$CuFeO_2$/ZIF-67 (4 h)	3321.904	3078.398
$CuFeO_2$/ZIF-67 (6 h)	8609.697	6271.438
$CuFeO_2$/ZIF-67 (8 h)	22073.600	9351.519
$CuFeO_2$/ZIF-67 (10 h)	5699.618	6110.161

ACKNOWLEDGEMENTS

This research is financially supported by the National Natural Science Foundation of China (Grant No. 22102140), the Natural Science Foundation of Jiangsu Province (Grant No. BK20211602), the Six Talent Peaks Project in Jiangsu Province (2019-XCL-101), the Specially-Appointed Professor Plan in Jiangsu Province, and Qing Lan Project of Yangzhou University.

REFERENCES

(1) Miyamura, H.; Matsubara, R.; Miyazaki, Y.; Kobayashi, S. Aerobic Oxidation of Alcohols at Room Temperature and Atmospheric Conditions Catalyzed by Reusable Gold Nanoclusters Stabilized by the Benzene Rings of Polystyrene Derivatives. *Angewandte Chemie International Edition* **2007**, *46* (22), 4151–4154. https://doi.org/10.1002/anie.200700080.

(2) Feng, W.; Wu, G.; Li, L.; Guan, N. Solvent-Free Selective Photocatalytic Oxidation of Benzyl Alcohol over Modified TiO2. *Green Chem.* **2011**, *13* (11), 3265–3272. https://doi.org/10.1039/C1GC15595D.

(3) Zheng, C.; He, G.; Xiao, X.; Lu, M.; Zhong, H.; Zuo, X.; Nan, J. Selective Photocatalytic Oxidation of Benzyl Alcohol into Benzaldehyde with High Selectivity and Conversion Ratio over Bi4O5Br2 Nanoflakes under Blue LED Irradiation. *Applied Catalysis B: Environmental* **2017**, *205*, 201–210. https://doi.org/10.1016/j.apcatb.2016.12.026.

(4) Tu, S.; Zhang, Y.; Reshak, A. H.; Auluck, S.; Ye, L.; Han, X.; Ma, T.; Huang, H. Ferroelectric Polarization Promoted Bulk Charge Separation for Highly Efficient CO2

Photoreduction of SrBi4Ti4O15. *Nano Energy* **2019**, *56*, 840–850. https://doi.org/10.1016/j.nanoen.2018.12.016.

(5) Zhang, J.; Zhang, M.; Sun, R.-Q.; Wang, X. A Facile Band Alignment of Polymeric Carbon Nitride Semiconductors to Construct Isotype Heterojunctions. *Angewandte Chemie International Edition* **2012**, *51* (40), 10145–10149. https://doi.org/10.1002/anie.201205333.

(6) Bian, J.; Zhang, Z.; Feng, J.; Thangamuthu, M.; Yang, F.; Sun, L.; Li, Z.; Qu, Y.; Tang, D.; Lin, Z.; Bai, F.; Tang, J.; Jing, L. Energy Platform for Directed Charge Transfer in the Cascade Z-Scheme Heterojunction: CO2 Photoreduction without a Cocatalyst. *Angewandte Chemie International Edition* **2021**, *60* (38), 20906–20914. https://doi.org/10.1002/anie.202106929.

(7) Li, Y.; Wu, Q.; Chen, Y.; Zhang, R.; Li, C.; Zhang, K.; Li, M.; Lin, Y.; Wang, D.; Zou, X.; Xie, T. Interface Engineering Z-Scheme Ti-Fe2O3/In2O3 Photoanode for Highly Efficient Photoelectrochemical Water Splitting. *Applied Catalysis B: Environmental* **2021**, *290*, 120058. https://doi.org/10.1016/j.apcatb.2021.120058.

(8) Li, Y.; Wu, Q.; Zhang, K.; Hu, B.; Lin, Y.; Wang, D.; Xie, T. Boosting Photocatalytic Oxygen Evolution: Purposely Constructing Direct Z-Scheme Photoanode by Modulating the Interface Electric Field. *Chemical Research in Chinese Universities* **2020**, *36* (6), 1059–1067. https://doi.org/10.1007/s40242-020-0278-9.

(9) Zhao, Z.-J.; Liu, S.; Zha, S.; Cheng, D.; Studt, F.; Henkelman, G.; Gong, J. Theory-Guided Design of Catalytic Materials Using Scaling Relationships and Reactivity Descriptors. *Nature Reviews Materials* **2019**, *4* (12), 792–804. https://doi.org/10.1038/s41578-019-0152-x.

(10) Yu, H.; Li, J.; Zhang, Y.; Yang, S.; Han, K.; Dong, F.; Ma, T.; Huang, H. Three-in-One Oxygen Vacancies: Whole Visible-Spectrum Absorption, Efficient Charge Separation, and Surface Site Activation for Robust CO2 Photoreduction. *Angewandte Chemie International Edition* **2019**, *58* (12), 3880–3884. https://doi.org/10.1002/anie.201813967.

(11) Lin, Y.; Xu, Y.; Mayer, M. T.; Simpson, Z. I.; McMahon, G.; Zhou, S.; Wang, D. Growth of P-Type Hematite by Atomic Layer Deposition and Its Utilization for Improved Solar Water Splitting. *J. Am. Chem. Soc.* **2012**, *134* (12), 5508–5511. https://doi.org/10.1021/ja300319g.

(12) Sun, X.; Shi, L.; Huang, H.; Song, X.; Ma, T. Surface Engineered 2D Materials for Photocatalysis. *Chem. Commun.* **2020**, *56* (75), 11000–11013. https://doi.org/10.1039/D0CC04790B.

(13) Lai, C.; An, N.; Li, B.; Zhang, M.; Yi, H.; Liu, S.; Qin, L.; Liu, X.; Li, L.; Fu, Y.; Xu, F.; Wang, Z.; Shi, X.; An, Z.; Zhou, X. Future Roadmap on Nonmetal-Based 2D Ultrathin Nanomaterials for Photocatalysis. *Chemical Engineering Journal* **2021**, *406*, 126780. https://doi.org/10.1016/j.cej.2020.126780.

(14) Zhang, X.; Chen, A.; Chen, L.; Zhou, Z. 2D Materials Bridging Experiments and Computations for Electro/Photocatalysis. *Advanced Energy Materials* **2022**, *12* (4), 2003841. https://doi.org/10.1002/aenm.202003841.

(15) Xing, Z.; Hu, J.; Ma, M.; Lin, H.; An, Y.; Liu, Z.; Zhang, Y.; Li, J.; Yang, S. From One to Two: In Situ Construction of an Ultrathin 2D-2D Closely Bonded Heterojunction from a Single-Phase Monolayer Nanosheet. *J. Am. Chem. Soc.* **2019**, *141* (50), 19715–19727. https://doi.org/10.1021/jacs.9b08651.

(16) Liu, Z.; El-Demellawi, J. K.; Bakr, O. M.; Ooi, B. S.; Alshareef, H. N. Plasmonic Nb2CTx MXene-MAPbI3 Heterostructure for Self-Powered Visible-NIR Photodiodes. *ACS Nano* **2022**. https://doi.org/10.1021/acsnano.2c00558.

(17) Kang, U.; Choi, S. K.; Ham, D. J.; Ji, S. M.; Choi, W.; Han, D. S.; Abdel-Wahab, A.; Park, H. Photosynthesis of Formate from CO_2 and Water at 1% Energy Efficiency via Copper Iron Oxide Catalysis. *Energy & Environmental Science* **2015**, *8* (9), 2638–2643. https://doi.org/10.1039/C5EE01410G.

(18) Jiang, C.-M.; Reyes-Lillo, S. E.; Liang, Y.; Liu, Y.-S.; Liu, G.; Toma, F. M.; Prendergast, D.; Sharp, I. D.; Cooper, J. K. Electronic Structure and Performance Bottlenecks of CuFeO2 Photocathodes. *Chem. Mater.* **2019**, *31* (7), 2524–2534. https://doi.org/10.1021/acs.chemmater.9b00009.

(19) Li, Z.; Zhang, X.; Kang, Y.; Yu, C. C.; Wen, Y.; Hu, M.; Meng, D.; Song, W.; Yang, Y. Interface Engineering of Co-LDH@MOF Heterojunction in Highly Stable and Efficient Oxygen Evolution Reaction. *Advanced Science* **2021**, *8* (2), 2002631. https://doi.org/10.1002/advs.202002631.

(20) Xu, C.; Jiang, T.; Wu, Z.; Zhou, W.; Zhang, X.; Guo, T.; Wu, L.; Xue, H. P-Type CuFeO2 Nanoflakes Prepared by Sodium Alginate-Assisted Hydrothermal Method for Photoelectrochemical Water Reduction. *Journal of Materials Science* **2018**, *53* (17), 12407–12412. https://doi.org/10.1007/s10853-018-2500-4.

(21) Liu, Q.-L.; Zhao, Z.-Y.; Zhao, R.-D.; Yi, J.-H. Fundamental Properties of Delafossite CuFeO2 as Photocatalyst for Solar Energy Conversion. *Journal of Alloys and Compounds* **2020**, *819*, 153032. https://doi.org/10.1016/j.jallcom.2019.153032.

(22) Pattengale, B.; Yang, S.; Ludwig, J.; Huang, Z.; Zhang, X.; Huang, J. Exceptionally Long-Lived Charge Separated State in Zeolitic Imidazolate Framework: Implication for Photocatalytic Applications. *J. Am. Chem. Soc.* **2016**, *138* (26), 8072–8075. https://doi.org/10.1021/jacs.6b04615.

(23) Kong, Z.-C.; Liao, J.-F.; Dong, Y.-J.; Xu, Y.-F.; Chen, H.-Y.; Kuang, D.-B.; Su, C.-Y. Core@Shell CsPbBr3@Zeolitic Imidazolate Framework Nanocomposite for Efficient Photocatalytic CO2 Reduction. *ACS Energy Lett.* **2018**, *3* (11), 2656–2662. https://doi.org/10.1021/acsenergylett.8b01658.

(24) Yuan, X.; Mu, Q.; Xue, S.; Su, Y.; Zhu, Y.; Sun, H.; Deng, Z.; Peng, Y. Polypyrrole Reinforced ZIF-67 with Modulated Facet Exposure and Billion-Fold Electrical Conductivity Enhancement towards Robust Photocatalytic CO2 Reduction. *Journal of Energy Chemistry* **2021**, *60*, 202–208. https://doi.org/10.1016/j.jechem.2020.12.025.

(25) Sambur, J. B.; Chen, T.-Y.; Choudhary, E.; Chen, G.; Nissen, E. J.; Thomas, E. M.; Zou, N.; Chen, P. Sub-Particle Reaction and Photocurrent Mapping to Optimize Catalyst-Modified Photoanodes. *Nature* **2016**, *530* (7588), 77–80. https://doi.org/10.1038/nature16534.

(26) Hesari, M.; Mao, X.; Chen, P. Charge Carrier Activity on Single-Particle Photo(Electro)Catalysts: Toward Function in Solar Energy Conversion. *J. Am. Chem. Soc.* **2018**, *140* (22), 6729–6740. https://doi.org/10.1021/jacs.8b04039.

(27) Luo, Z.; Ye, X.; Zhang, S.; Xue, S.; Yang, C.; Hou, Y.; Xing, W.; Yu, R.; Sun, J.; Yu, Z.; Wang, X. Unveiling the Charge Transfer Dynamics Steered by Built-in Electric Fields in BiOBr Photocatalysts. *Nature Communications* **2022**, *13* (1), 2230. https://doi.org/10.1038/s41467-022-29825-0.

(28) Tachikawa, T.; Yamashita, S.; Majima, T. Evidence for Crystal-Face-Dependent TiO2 Photocatalysis from Single-Molecule Imaging and Kinetic Analysis. *J. Am. Chem. Soc.* **2011**, *133* (18), 7197–7204. https://doi.org/10.1021/ja201415j.
(29) Ohno, T.; Sarukawa, K.; Matsumura, M. Crystal Faces of Rutile and Anatase TiO2 Particles and Their Roles in Photocatalytic Reactions. *New J. Chem.* **2002**, *26* (9), 1167–1170. https://doi.org/10.1039/B202140D.
(30) Yang, X.; Wang, D. Photocatalysis: From Fundamental Principles to Materials and Applications. *ACS Appl. Energy Mater.* **2018**, *1* (12), 6657–6693. https://doi.org/10.1021/acsaem.8b01345.
(31) Takanabe, K. Photocatalytic Water Splitting: Quantitative Approaches toward Photocatalyst by Design. *ACS Catal.* **2017**, *7* (11), 8006–8022. https://doi.org/10.1021/acscatal.7b02662.
(32) Lin, R.; Wan, J.; Xiong, Y.; Wu, K.; Cheong, W.; Zhou, G.; Wang, D.; Peng, Q.; Chen, C.; Li, Y. Quantitative Study of Charge Carrier Dynamics in Well-Defined WO3 Nanowires and Nanosheets: Insight into the Crystal Facet Effect in Photocatalysis. *J. Am. Chem. Soc.* **2018**, *140* (29), 9078–9082. https://doi.org/10.1021/jacs.8b05293.
(33) Sigle, D. O.; Zhang, L.; Ithurria, S.; Dubertret, B.; Baumberg, J. J. Ultrathin CdSe in Plasmonic Nanogaps for Enhanced Photocatalytic Water Splitting. *J. Phys. Chem. Lett.* **2015**, *6* (7), 1099–1103. https://doi.org/10.1021/acs.jpclett.5b00279.
(34) Takata, T.; Jiang, J.; Sakata, Y.; Nakabayashi, M.; Shibata, N.; Nandal, V.; Seki, K.; Hisatomi, T.; Domen, K. Photocatalytic Water Splitting with a Quantum Efficiency of Almost Unity. *Nature* **2020**, *581* (7809), 411–414. https://doi.org/10.1038/s41586-020-2278-9.
(35) Li, C.; Liu, J.; Li, H.; Wu, K.; Wang, J.; Yang, Q. Covalent Organic Frameworks with High Quantum Efficiency in Sacrificial Photocatalytic Hydrogen Evolution. *Nature Communications* **2022**, *13* (1), 2357. https://doi.org/10.1038/s41467-022-30035-x.
(36) Ferri, M.; Elliott, J.; Farnesi Camellone, M.; Fabris, S.; Piccinin, S. Thermodynamic Stability and Native Point Defects of CuFeO2 Photocathodes in Dry and Electrochemical Environments. *J. Phys. Chem. C* **2019**, *123* (49), 29589–29598. https://doi.org/10.1021/acs.jpcc.9b08957.
(37) Tao, L.; Lin, C.-Y.; Dou, S.; Feng, S.; Chen, D.; Liu, D.; Huo, J.; Xia, Z.; Wang, S. Creating Coordinatively Unsaturated Metal Sites in Metal-Organic-Frameworks as Efficient Electrocatalysts for the Oxygen Evolution Reaction: Insights into the Active Centers. *Nano Energy* **2017**, *41*, 417–425. https://doi.org/10.1016/j.nanoen.2017.09.055.
(38) Pylypenko, S.; Mukherjee, S.; Olson, T. S.; Atanassov, P. Non-Platinum Oxygen Reduction Electrocatalysts Based on Pyrolyzed Transition Metal Macrocycles. *Electrochimica Acta* **2008**, *53* (27), 7875–7883. https://doi.org/10.1016/j.electacta.2008.05.047.

SYNOPSIS.

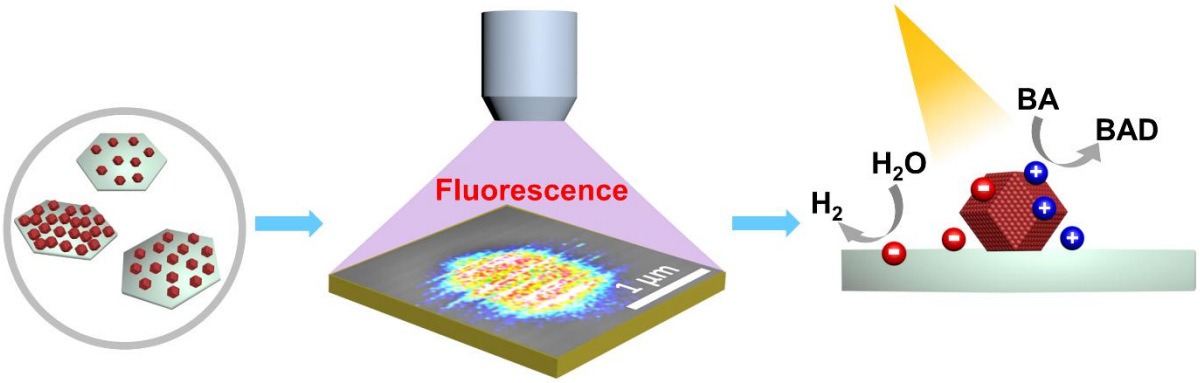

An experimental descriptor, the average fluorescence intensity (AFI), was developed to rapidly identify the high-performance photocatalyst using fluorescence microscopic visualization.